Design and Testing of a Low-Cost MEMS IMU Cluster for SmallSat Applications

Daniel R. Greenheck, Robert H. Bishop, Eric M. Jonardi
Marquette University
Milwaukee, WI 53233; 715-571-5690
dgreenheck@gmail.com

John A. Christian
West Virginia University
Morgantown, WV 26506

ABSTRACT

Small satellite missions are characterized by tight constraints on cost, mass, power, and volume that generally make them unable to fly inertial measurement units (IMUs) required for orbital missions demanding precise orientation and positioning. Instead, small satellite missions typically fly low-cost micro-electro-mechanical system (MEMS) IMUs. The performance characteristics of MEMS IMUs make them ineffectual in many spaceflight applications when employed in a single IMU system configuration. The challenge for small satellite designs aiming to tackle more aggressive missions is to creatively employ advanced software algorithms coupled with embedded system architectures to create an effective precision IMU from clusters of low-cost MEMS IMUs. The objective of this work is to develop and demonstrate a MEMS IMU cluster whose composite output provides high performance while remaining within the mass, power, and volume constraints of a 1U CubeSat. Successfully achieving this objective will represent a new class of inertial navigation performance for the small satellite platform. We investigate the practical issues associated with implementing an IMU cluster in a form factor suitable for use on a 1U CubeSat. The results show that in general, simple averaging of the sensor outputs approaches the predicted square root of *N* improvement in performance for the RMS noise and bias stability of the sensors. However, some sensors exhibited lower performance improvements than other sensors, indicating a higher correlation between individual sensors.

INTRODUCTION

Definitions and Applications

An inertial measurement unit (IMU) is a device capable of sensing non-gravitational accelerations and angular rates that can be employed to propagate vehicle position, velocity, and attitude between external updates (e.g. Global Positioning System or a star tracker) [1]. This can be accomplished by measuring accelerations acting on the body as well as tracking any changes in the orientation of the body to allow the reference frame of the body to be transformed back to an inertial frame.

Accelerations are most often measured using *linear accelerometers*. A linear accelerometer outputs an analog or digital electrical signal proportional to the linear acceleration experienced by the sensor along a predefined axis. An accelerometer is typically selected that measures accelerations along three mutually orthogonal axes to provide a full description of the accelerations acting upon the body. A *gyroscope* (or gyro) is an instrument able to track changes in orientation over time. Similar to the accelerometer, the change in orientation is measured relative to a set of three mutually orthogonal axes [2]. These two sensors allow the complete state of a body (position, velocity, orientation) to be determined.

Vehicle navigation is one of the primary applications of an IMU. While this work focuses on satellite applications, IMUs are also extensively used in robotics, self-driving cars, aircraft, nautical vessels and a host of other vehicles. Outputs from the IMU are utilized by signal processing and control algorithms from which changes in orientation and velocity may be sensed. For many space applications, the gyros play a more important role than the accelerometers, except during propulsive maneuvers. Otherwise, in low-Earth orbit, the linear accelerometers only sense aerodynamic drag and these accelerations may be small compared to the noise on the acceleration measurements. Thus, it is common for an acceleration threshold to be set below which the output of the accelerometer is not considered and spacecraft translational motion is described by orbital mechanics.

An IMU can be used in conjunction with external navigation updates, such as GPS, or act independently, resulting in a completely self-contained navigation solution. An example of when self-contained navigation is often employed is during spacecraft re-entry. During hypersonic re-entry of a spacecraft, a plasma sheath surrounds the vehicle as a result of the extreme heating of the air generated by strong shock waves at the vehicle leading edges. The plasma, consisting of ions and free electrons, can reflect and attenuate the propagation of electromagnetic waves, including those at frequencies used for radio communications. This results in a "communication blackout" for some period of time during re-entry. The spacecraft must rely on inertial navigation during this time since external navigational updates cannot be communicated to the spacecraft [3,4].

Although the concept of a completely self-contained navigation system is enticing, one disadvantage of IMUs is that navigation errors tend to quickly build up over time. Determining the position requires integrating the measured acceleration twice with respect to time. If a constant bias is present in the linear acceleration measurement, it would result in a position error that grows quadratically with time. Similarly, the output of the gyro must be integrated once with respect to time in order to determine the orientation. A constant bias error in the rate of change of the orientation measurement would result in a ramp error in the orientation measurement. Because of this, much effort has been put in to developing new technologies to minimize the various errors found in inertial navigation systems.

Accelerometer and Gyroscope Technologies

Different types of inertial sensor technologies for both accelerometers and gyros have been developed to mitigate errors, each having different tradeoffs between performance, mass, volume and power consumption. The three most common types of gyroscopes are the *ring laser gyroscope (RLG), the fiber optic gyroscope (FOG), and the micro-machined electromechanical system (MEMS) gyroscope.*

Mirrors are aligned in the RLG to produce a closed light path. Two counter-propagating laser beams are directed along this path. As the apparatus is rotated about the axis normal to the plane of the light path, the path length of each beam is altered resulting in a phase difference which can be measured by allowing the two beams to undergo interference. This phase difference is proportional to the angular rate [5].

FOGs operate on a similar principle. A coil of fiber optic cable is wrapped around a cylindrical drum. Light is directed through a beam splitter creating two countercurrent light paths. As the drum rotates about its axis, the transmit time for each path is altered, resulting in a phase difference which can be detected at the point of entry via an interference measurement. This phase difference can be measured and related to the angular rate [5].

One of the technologies developed in recent years is the MEMS gyroscope. These sensors are inexpensive, small and have few moving parts [5]. Although there are several sub-classifications within the grouping of MEMS gyroscopes, only Coriolis vibratory gyroscopes will be considered here. In a single-axis configuration, two proof masses are attached on either side of a fixed platform. The masses are driven at a specific frequency along the horizontal plane. If a rotation is applied to the axis normal to the plane, the Coriolis force causes the two masses to deflect in opposite directions. A differential capacitive measurement results in a value corresponding to the angular rate [5].

Several accelerometer technologies include the *force-feedback accelerometer,* the *vibratory accelerometer* and the *pendulous mass MEMS accelerometer.* The mechanical force-feedback accelerometer consists of a pendulum with an attached proof mass. Initially, the pendulum is at a standstill in the equilibrium position. As an acceleration is applied, the pendulum moves from its equilibrium position. The deviation is directly proportional to the applied acceleration.

The *vibratory accelerometer* has two quartz crystal beams positioned back to back, each supporting a proof mass. The beams vibrate at their own resonant frequency. When an acceleration is applied along the sensitive axis, one beam undergoes compression while the other undergoes expansion, altering the resonant frequency. The difference in resonant frequencies is directly proportional to the applied acceleration.

There are two main types of MEMS accelerometers: *pendulous mass* and *vibrating beam*. Only pendulous mass accelerometers will be considered here. In this configuration, a polysilicon structure is suspended over a silicon substrate by a set of polysilicon springs, creating a differential capacitor. As the structure deflects due to accelerative forces, the capacitance of the differential capacitor changes. The magnitude and direction of the acceleration can be determined via phase-sensitive demodulation techniques [5,6].

Aims of Study

In this study, we seek to demonstrate that placing MEMS sensors in a cluster configuration results in the predicted improvements [7]. The cluster configuration consists of placing multiple MEMS sensors on a single

circuit board and synthesizing their outputs to create a single output which has improved performance characteristics over that of a single MEMS sensor. We examine the benefits of simple averaging of the sensor outputs.

A custom board was designed and fabricated to test the objective of fusing many simultaneous MEMS IMU measurements. What follows is a description of the physical board layout, the process used to calibrate the sensors, and a comparison between the RMS noise and bias stability of a single MEMS sensor and a custom MEMS IMU cluster. Additionally, the MEMS IMU cluster described here is compared to a number of current IMUs on the market of varying degrees of performance. A comparison that scales the performance by the power and mass of the devices is also included, as these constraints are often just as important as the performance of the IMU in small satellite applications.

BOARD DESIGN AND LAYOUT

The IMU is 10 cm x 10 cm circuit board designed to fit within a 1U CubeSat form factor. The sensor cluster is made up of 16 individual sensor groups. Each sensor group contains two dual-axis analog MEMS gyros (ST Microelectronics LPY410AL) as well as a single tri-axial analog MEMS accelerometer (Analog Devices ADXL335), for a total of 32 gyros and 16 accelerometers on a single board, or 112 individual inertial measurements. Dual-axis gyros were chosen instead of tri-axial because the selection of single-package tri-axial analog output MEMS gyros is limited. Each pair of gyros is perpendicularly aligned to provide a measurement of all three axes. The seven analog sensor outputs of each sensor channel are sampled sequentially by a high speed 16-bit analog-to-digital converter (ADC). The high sampling speed of the ADC (Texas Instruments ADS8332) compared to the maximum output bandwidth of the analog sensors (500kSPS vs 1.6kHz) allows near-simultaneous sampling of the seven sensor outputs within each sensor channel.

Each sensor channel has its own ADC, allowing simultaneous sampling of a single IMU axis (e.g. the x-axis on the MEMS accelerometer) across all sensor channels. An op-amp buffer in a unity gain configuration is placed between each sensor output and the ADC as a precaution to ensure sufficient drive strength into the ADC inputs.

A FPGA (Lattice XP2-8) located at the center of the board serves as a massively parallel I/O processor to simultaneously acquire data from the ADCs. The FPGA has two onboard decimation units to control the rate of data output. Each will discard N of $N+1$ data sets, where N is the setting. At present, the FPGA collects the data in parallel from the sensor channels and transmits it serially over USB; all processing is done via an external processing unit. However, the authors would like to mention that the FPGA has sufficient internal logic resources to implement signal filtering and navigation algorithms within the FPGA itself in the future. With the addition of an on-board wireless system, this would eliminate the need for an external processing unit. Our current goal of determining how the performance of a MEMS IMU cluster compares with single MEMS gyro and accelerometer does not require on board processing.

A UART/FIFO IC (FTDI FT2232HL) serves as a communication bridge between the FPGA and an external Mini-USB connection. The connection is used to both collect data via a host computer as well as controlling the internal settings of the IMU. A second Mini-USB port provides auxiliary power to the board as the power consumption of the board exceeds the 500 mA maximum limit for USB.

Figure 1 illustrates the rendered exploded view of IMU assembly and custom enclosure and Figure 2 shows the rapid prototype of IMU enclosure. The enclosure was designed to contain the entire IMU cluster in preparation for sounding rocket flight testing. The schematic of the integrated system is shown in Figure 3. The main elements of the unit are the battery, voltage regulator and charging circuit, the MEMS IMU cluster, and the Raspberry Pi processor. We collect data through a wireless dongle to a remote laptop. We currently do not perform significant calculations on the onboard processor, but that is a target for our coning and sculling algorithms as we further develop the IMU cluster.

External Processing

External processing is carried out on a Raspberry Pi Model B (512 MB of RAM, Broadcom BCM2835 700MHz ARM1176JZFS processor). The Raspberry Pi was chosen for the prototype due to its simplicity, wireless capabilities and small form factor. Currently, the Raspberry Pi receives the data from the IMU board over a serial connection and transmits it wirelessly to a host computer via TCP/IP connection. The wireless connection is established over WiFi using an 802.11n wireless adapter (Edimax EW-7811Un).

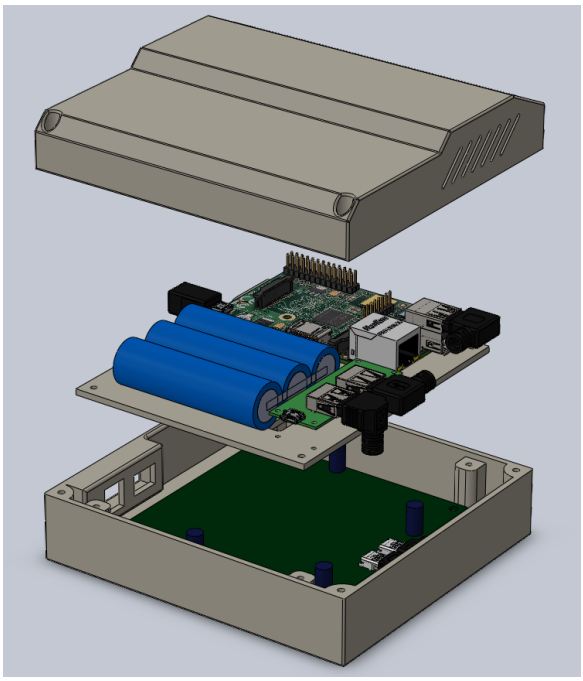

Figure 1: Rendered exploded view of IMU assembly and custom enclosure

Figure 2: Rapid prototype of IMU enclosure

Power

The entire assembly is powered by an off-the-shelf consumer Lithium-polymer battery pack with a capacity of 6600 mAh and regulated output voltage of 5V. The battery pack has two USB-A outputs which provide 1A and 2A of current. There is also a Micro USB port on the side for charging the battery pack. This battery pack was chosen because of its sufficiently small form factor and weight, as well easily interfacing with the USB connections on the MEMS IMU board and the Raspberry Pi. The battery is able to power the IMU and Raspberry Pi for approximately 4-5 hours at full charge. Future work includes eliminating the USB connections

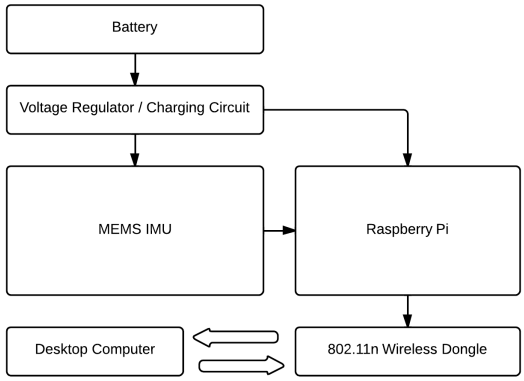

Figure 3: Flow diagram of IMU connections

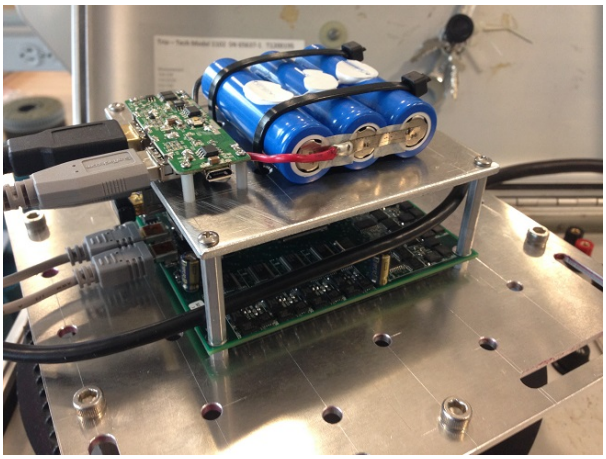

Figure 4: IMU test fixture mounted on rate table

as the cables are bulky and add unnecessary weight to the assembly. Linear power supplies were used on the IMU board instead of switching supplies to minimize electrical noise. A number of additional noise reduction techniques were also employed to minimize electrical noise as much as possible.

CALIBRATION

Measurement Setup

Calibration of the IMU board was performed on a single-axis rate table (Trio-Tech Model 1102). The rate table itself was calibrated by a trained technician before testing. Before any measurements were taken, the table was first leveled using a built-in bubble level on top of the rate table. The test setup is shown in Figure 4.

Data Collection

Sensor data was collected at 100 °/s clockwise, 100 °/s counter-clockwise, and at zero rate. Data was recorded in six different orientations: each sensing axis of the IMU was aligned to be parallel with the gravitational vector, as well as anti-parallel. Accelerometer data was

collected at zero rate with the gravitational force being the input acceleration.

Accelerometer Calibration

The bias level, scale factors, and misalignment for each individual accelerometer were calculated using the test procedures outlined in [8]. The bias level was calculated by mounting each sensing axis of the accelerometers both parallel with the gravitational vector parallel as well as anti-parallel, for a total of six orientations. For a single axis, the bias level is given by

$$B_a = \frac{a_+ + a_-}{2} \tag{1}$$

where a_+ is the digital output of the accelerometer with an input acceleration of $+g$ and a_- is the digital output of the accelerometer with an input acceleration of $-g$. The units of B_a are given in μg. The scale factor for a single axis is calculated similarly by

$$S_a = \frac{a_+ - a_-}{2B_a} \tag{2}$$

with the units of S_a given in $\left(\frac{LSB}{\mu g}\right)$.

Calculation of the inter-axial error, or misalignment angles, requires four separate measurements. Using the x-axis as an example, the x-axis is first aligned horizontally with the y-axis pointing downwards. The output of the x-axis is recorded ($a_{x,+y}$). The same procedure is repeated, except with the y-axis pointing upwards. The output of the x-axis is recorded ($a_{x,-y}$). The misalignment angle with respect to the y-axis is then given by (3). Equation (4) follows similarly.

$$\delta_{a,xy} = \frac{a_{x,+y} - a_{x,-y}}{2S_a} \tag{3}$$

$$\delta_{a,xz} = \frac{a_{x,+z} - a_{x,-z}}{2S_a} \tag{4}$$

Knowing the bias level, scale factor and misalignment angles for each individual sensor allow for a basic calibration of the IMU. However, this calibration does not take into account environmental thermal fluctuations. To minimize this effect, the data was acquired at night when the temperature of the room was the most stable. The parameters can be combined into a model of the accelerometer, given by

$$\boldsymbol{a}_{true} = (\mathbf{I} + \boldsymbol{S}_a)(\mathbf{I} + \boldsymbol{\Gamma}_a)(\boldsymbol{a}_{meas} + \boldsymbol{B}_a) \tag{5}$$

where $\boldsymbol{a}_{meas}$ is a vector of the digital outputs of the accelerometer, $\boldsymbol{a}_{true}$ is the acceleration truth vector, $\boldsymbol{B}_a$ is a vector of the accelerometer bias values for each axis, $\boldsymbol{S}_a$ is the accelerometer sensitivity matrix and $\boldsymbol{\Gamma}_a$ is the accelerometer misalignment matrix. The sensitivity matrix and misalignment matrix are defined below

$$\mathbf{S}_a = \begin{pmatrix} S_{a,x} & 0 & 0 \\ 0 & S_{a,y} & 0 \\ 0 & 0 & S_{a,z} \end{pmatrix} \tag{6}$$

$$\boldsymbol{\Gamma}_a = \begin{pmatrix} 0 & \delta_{a,xy} & \delta_{a,xz} \\ \delta_{a,yx} & 0 & \delta_{a,yz} \\ \delta_{a,zx} & \delta_{a,zy} & 0 \end{pmatrix} \tag{7}$$

Gyroscope Calibration

The process of calibrating the gyros is analogous to the process of calibrating the accelerometers [9]. The equations for the x-axis bias level, scale factor and misalignment angles are given by

$$B_g = \frac{\omega_+ + \omega_-}{2} \tag{8}$$

$$S_g = \frac{\omega_+ - \omega_-}{2B_g} \tag{9}$$

$$\delta_{g,xy} = \frac{\omega_{x,+y} - \omega_{x,-y}}{2S_g} \tag{10}$$

$$\delta_{g,xz} = \frac{\omega_{x,+z} - \omega_{x,-z}}{2S_g} \tag{11}$$

where ω_+ is a positive rotation about the axis being sensed, ω_- is a rotation rate equal in magnitude to ω_+ except with opposite sign, $\omega_{x,+y}$, $\omega_{x,-y}$ are positive and negative rotations of equal magnitude about the y-axis, respectively, and $\omega_{x,+z}$, $\omega_{x,-z}$ are positive and negative rotations of equal magnitude about the z-axis, respectively. The equations for the y and z axes follow similarly. The parameters can be combined into a model of the gyroscope, given by

$$\boldsymbol{\omega}_{true} = (\mathbf{I} + \boldsymbol{S}_g)(\mathbf{I} + \boldsymbol{\Gamma}_g)(\boldsymbol{\omega}_{meas} + \boldsymbol{B}_g) \tag{12}$$

where $\boldsymbol{\omega}_{meas}$ is a vector of the digital outputs of the gyro, $\boldsymbol{B}_g$ is a vector of the gyro bias values for each axis, $\boldsymbol{S}_g$ is the gyro sensitivity matrix and $\boldsymbol{\Gamma}_g$ is the gyro misalignment matrix and $\boldsymbol{\omega}_{true}$ is the angular rate truth vector.

EXPERIMENT DESIGN

Introduction

When comparing the performance of IMUs, there are often several standard metrics used to facilitate a standard comparison between different technologies. *Bias stability* is the deviation from the mean value over a period of time given a constant input. With units of deg/hr for gyros or μg for accelerometers, a higher value for bias stability indicates that the bias has large fluctuations about the mean. Such fluctuations have implications on how IMU biases should be treated in Kalman filters that may process these measurements. *Rate noise density* is an indication of noise at the output of the sensor. The faster a sensor is sample, the more the noise will affect the final measurement. For gyros, this measure is often expressed as *angle random walk* (ARW) in units of degrees per root hour. ARW is the standard deviation of the error introduced by integrating noisy gyro measurements. *Scale factor stability* is a measure of the deviation of the scale factor for constant conditions over time and between different runs. Finally, *non-orthogonality* refers to the errors in the alignment of the sensor axes. This includes angular deviations of the axes from their true orientation as well as inter-axial angular errors.

For this study, the authors choose to experimentally determine bias stability and noise characteristics for both a single MEMS gyro/accelerometer, as well as the MEMS cluster.

RMS Noise

For a deterministic signal with additive zero-mean Gaussian noise which is uncorrelated with the signal, the improvement in the signal to noise ratio (SNR) by averaging N separate sample records is given by

$$SNR = \sqrt{N}\frac{S}{\sigma} \tag{13}$$

Since the IMU cluster has N=16 sensor groups that will be averaged together, our expectation is that the improvement in bias stability and noise will be on the order of $\sqrt{N}$ or a factor of 4. Because we are using multiples of the same sensor, not all of the noise sources will be completely uncorrelated. Therefore, the actual improvement is expected to be less than what theory predicts.

Method for Determining Bias Stability

The bias stability was calculated by creating an Allan variance plot for each individual sensor as well as the sensor clusters. The Allan variance method is a way of separating out different noise sources which contribute to the overall signal noise. In basic terms, an Allan variance plot shows the variance of the noise as a function of the averaging time.

The Allan variance is calculated according to [3] using the following formula

$$\sigma_a^2(\Delta t) = \frac{1}{2(N-1)}\sum_{j=1}^{N-1}\left(x_j - x_{j-1}\right)^2 \tag{14}$$

where $x_i, i = 1, \dots, N$ is the time series data and Δt is the sample time. Then a new sequence is defined

$$y_j = \frac{x_{2j} + x_{2j+1}}{2}, j = 0,1, \dots, \left\lfloor\frac{N}{2}\right\rfloor \tag{15}$$

and the Allan variance $\sigma_a^2(2\Delta t)$ is computed for that sequence. This process continues for longer and longer averaging times until a new y_j can no longer be formed. The square root of the Allan variance is then plotted on a log-log plot for analysis. Although it will not be shown here, the bias stability can be determined by looking at the minimum point on the Allan deviation curve.

Experimental Setup

The IMU cluster assembly was mounted to the rate table to provide a flat surface for testing. The negative z-axis of the IMU was aligned parallel with the gravitational vector. The onboard decimation units were set to produce a data output rate of 18.9 Hz. Data was continuously collected for eight hours, resulting in N = 545410 data points for each of the 112 sensor axes.

RESULTS AND DISCUSSION

RMS Noise

Figures 5 and 6 illustrate the difference in RMS noise between a single MEMS sensor and the sensor cluster for each axis of the gyros and accelerometers, respectively. The results are summarized in Table 1. The first column of Table 1 shows the RMS noise for a single sensor, the second column shows the RMS noise for the sensor cluster and the final column shows the ratio between the single sensor value and the sensor cluster value.

The authors would like to point out that for the ADXL335 accelerometer, the noise density specified for the z-axis of the accelerometer (referred to as the y-axis in this paper) is twice the value for the other two

axes. This explains why the RMS noise for the y-axis is twice that of the x and z axes.

As predicted, the improvement in noise is close to a factor of 4. The gyros showed the highest average performance realization. The gyro x-axis was the best performing, with a ratio of 3.9 between the single sensor performance and the cluster performance. The accelerometers also saw solid improvements in performance. The accelerometer z-axis did not perform as well as the other two axes (performance ratio = 2.7), suggesting that the correlation of the noise between sensors increases as they are subjected to an acceleration.

Table 1: RMS noise comparison between single sensor and sensor cluster

Accelerometer	Single (μg)	Cluster (μg)	Ratio
X-axis	3670	1060	3.5
Y-axis	6250	1800	3.5
Z-axis	3590	1330	2.7
Average	4500	1400	3.2
Gyroscope	**Single (deg/s)**	**Cluster (deg/s)**	**Ratio**
X-axis	0.418	0.108	3.9
Y-axis	0.393	0.109	3.6
Z-axis	0.422	0.111	3.8
Average	0.411	0.109	3.8

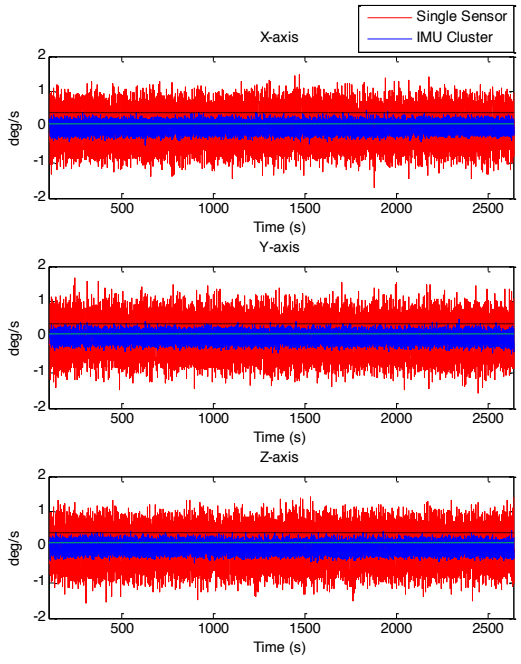

Figure 5: RMS noise of single MEMS gyro vs. MEMS cluster

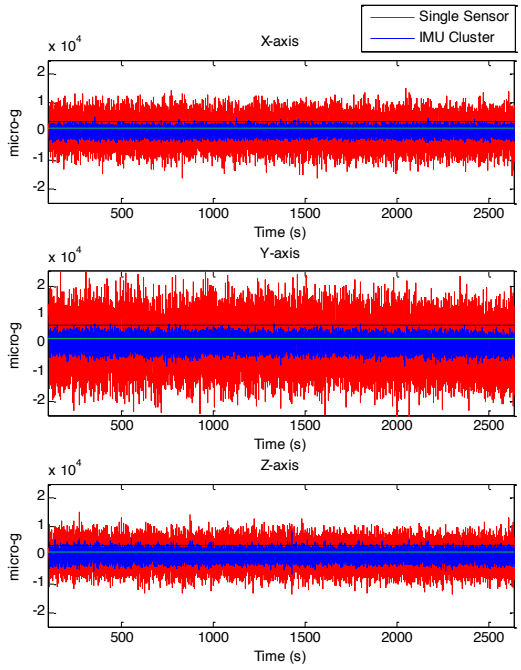

Figure 6: RMS noise of single MEMS accelerometer vs. MEMS cluster

Bias Stability

Figures 7 and 8 show the Allan variances for both the gyros and accelerometers in the single sensor and cluster configurations. For the case of a single sensor, the Allan variances for each individual sensor were calculated. For the cluster, the Allan variances were averaged across each group of sensors. The bias stability for each axis is indicated by a horizontal dotted line corresponding to the minimum of the graph. The results are summarized in Table 2. The average performance ratio for the accelerometers (ratio = 2.8) and the gyros (ratio = 3.0) shows a significant improvement via simple averaging. However, in comparison with the RMS noise, the performance improvements are not quite as pronounced. This may have been caused by changes in the bias due to temperature fluctuations since the experiment was not carried out in a controlled thermal environment. However, data was collected during the night to minimize any temperature fluctuations. The gyro y-axis stands out as the improvement ratio was only 2.4, compared to 3.3 for both the x-axis and z-axis. Data was recorded at different orientations to determine if this artifact was the result of *g*-dependent errors, but the results did not indicate any specific correlation with the orientation. The cause of the reduction in performance for the y-axis has not yet been determined.

The performance ratio for the other axes are consistent with the expected results given the fact that there are

unmodeled, correlated errors between the individual sensors.

Table 2: Bias stability comparison between a single sensor and sensor cluster

Accelerometer	Single (µg)	Cluster (µg)	Ratio
X-axis	62	23	2.7
Y-axis	152	56	2.7
Z-axis	61	21	2.8
Average	92	33	2.8
Gyroscope	**Single (deg/hr)**	**Cluster (deg/hr)**	**Ratio**
X-axis	29.5	9.0	3.3
Y-axis	25.3	10.6	2.4
Z-axis	26.6	8.0	3.3
Average	27.1	9.2	3.0

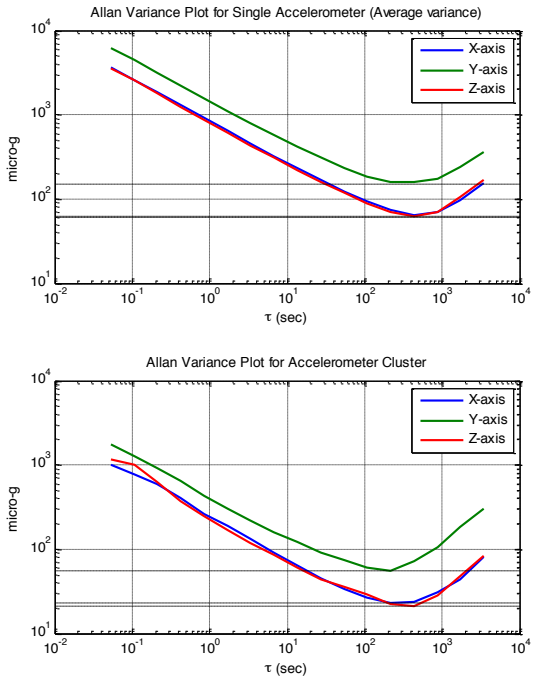

Figure 7: Allan variance of single MEMS accelerometer vs. MEMS cluster

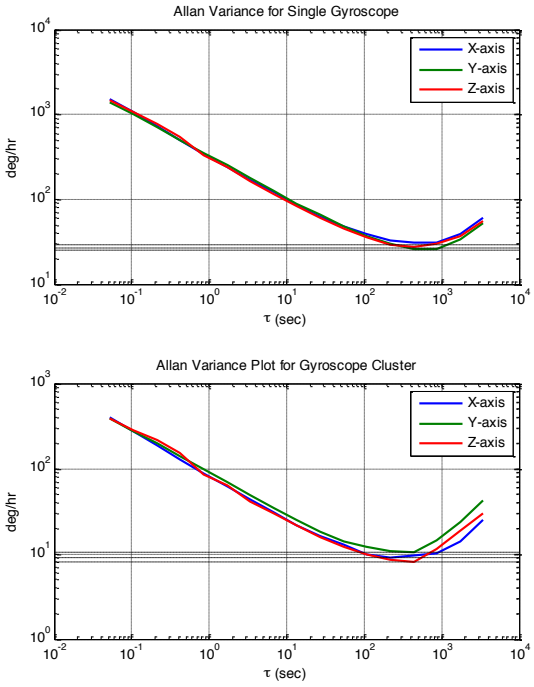

Figure 8: Allan variance of single MEMS gyro vs. MEMS cluster

Comparison with Other IMUs

A secondary aim of this work is to compare the performance of the MEMS IMU cluster to existing IMU sensors on the market. A direct comparison between a MEMS sensor and a RLG or FOG based sensor shows that much progress must be made before MEMS can be used in precision applications. However, for applications where quantities such as mass, power and volume are highly constrained, it is worth examining the tradeoff between mass, power, and performance. Figures 9 and 10 show the comparison between the MEMS IMU cluster and other types of IMUs on the market [10,11,12,13,14]. It is notable that the IMU cluster shown here is consistent with the mass, power, and performance trends seen with other IMUs.

By incorporating more precise MEMS IMUs, it is anticipated that the IMU cluster performance can be significantly improved with little change in the mass or power consumption. Replacing the analog sensors with digital output sensors would eliminate the need for the op-amps and ADCs, which would drastically reduce power consumption and shrink the board size due to fewer physical components being on the board.

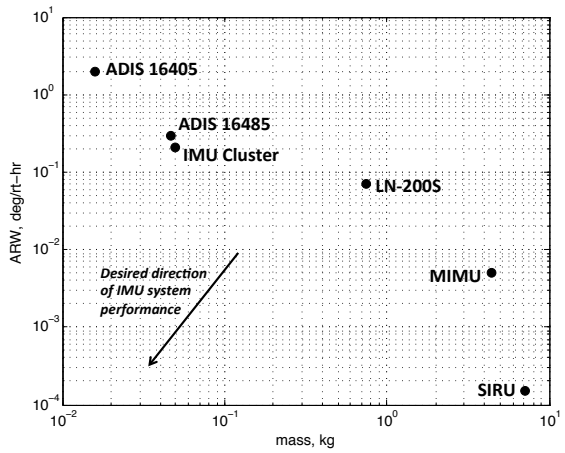

Figure 9: IMU Accuracy scaled by mass for the various types of IMUs

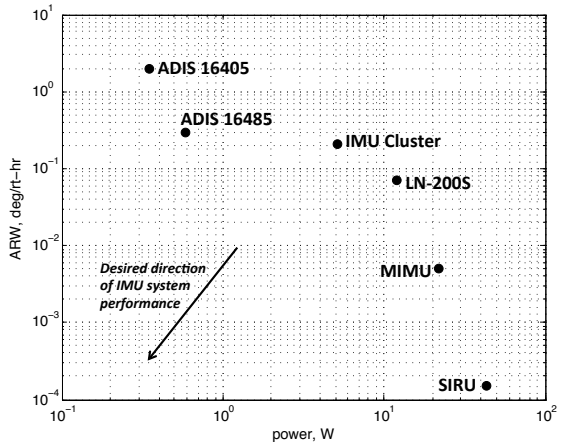

Figure 10: IMU Accuracy scaled by power for the various types of IMUs

CONCLUSION

Our results show that performance gains resulting from averaging of a cluster of MEMS sensors approaches the predicted performance. The improvement in RMS noise for a cluster of 16 MEMS accelerometers was on average 3.2x, while the improvement in RMS noise for a cluster of 16 MEMS gyros was 3.8x. Bias stability saw less of a performance improvement, with an average improvement of 2.8x for the accelerometers and 3.0x for the gyros. This suggests that correlation between bias stability errors across the individual sensors is higher than the correlation between errors due to random noise. The y-axis of the gyros also showed less improvement in bias stability when compared to the other gyro axes. Further experimentation will be needed to determine if this is a result of the test setup, the cluster configuration, or because of the actual sensors themselves.

Future work involves implementing signal processing techniques more advanced than simple averaging, such as using Kalman filtering. The board design could also be improved by using digital sensors instead of analog, which would reduce power consumption and reduce board size by eliminating the need for the buffers and the ADCs. Implementing the algorithms on the FPGA would also eliminate the need for an external processor, drastically reducing the mass, weight and volume of the current design.

Acknowledgments

This work was made possible by NASA cooperative agreement NNX13AQ79A with Marquette University under subcontract to West Virginia University.

References

1. El-Sheimy, N., Haiying Hou, and Xiaoji Niu, "Analysis and Modeling of Inertial Sensors Using Allan Variance," *IEEE Transactions on Instrumentation and Measurement*, Vol. 57, No. 1, 2008, pp. 140-149.
2. Britting, K.R., *Inertial Navigation Systems Analysis*, Wiley-Interscience, New York, 1971.
3. Nawrat, A., Jędrasiak K., Daniec K., and Koteras R., "Inertial Navigation Systems and its Practical Application," found in Chapter 10 of *New Approach of Indoor and Outdoor Localization Systems*, Fouzia Elbahhar and Atika Rivenq (Ed.), InTech, Croatia, 2012.
4. Hartunian, R.A., Stewart, G.E., Curtiss, T.J., Fergason, D., Seibold, R.W., and Shome, P., "Implications and Mitigation of Radio Frequency Blackout during Reentry of Reusable Launch Vehicles," AIAA 2007-6633, *AIAA Atmospheric Flight Mechanics Conference and Exhibit*, Hilton Head, SC, 2007
5. Titterton, D.H., and Weston, J.L., *Strapdown Inertial Navigation Technology,* 2nd Edition, IEE Radar, Sonar, Navigation and Avionics Series, The Institution of Engineering and Technology, 2005.
6. http://www.analog.com/static/imported-files/data_sheets/ADXL335.pdf
7. Crain, T.P., Bishop, R.H., and Brady, T, "Shifting the Inertial Navigation Paradigm with MEMS Technology," AAS 10-043, *33rd Guidance and Control Conference*, Breckenridge, CO, 2010.
8. "IEEE Standard Specification Format Guide and Test Procedure for Coriolis Vibratory Gyros,"

IEEE Standard 1431-2004, *IEEE Aerospace and Electronic Systems Society*, 2004, pp. 1-78.

9. "IEEE Standard Specification Format Guide and Test Procedure for Linear, Single-Axis, Non-Gyroscopic Accelerometers," IEEE Standard 1293-1998, 2011, pp. 1-249.
10. http://www51.honeywell.com/aero/common/documents/myaerospacecatalog-documents/MIMU.pdf
11. http://www.northropgrumman.com/Capabilities/SIRU/Documents/ssiru.pdf
12. http://www.analog.com/static/imported-files/data_sheets/ADIS16485.pdf
13. http://www.northropgrumman.com/Capabilities/LN200FOG/Documents/ln200s.pdf
14. http://www.analog.com/static/imported-files/data_sheets/ADIS16400_16405.pdf